

88  
79

## Fragmentation of suddenly heated liquids

James A. Blink and William G. Hoover

*Lawrence Livermore National Laboratory, Livermore, California 94550  
and Department of Applied Science, University of California, Davis, California 95616*

(Received 5 April 1985)

The rapid fragmentation of two-dimensional high-pressure disks of Lennard-Jones fluid was studied using molecular dynamics. The free expansion of 169-, 721-, 2611-, and 14 491-particle systems was studied for several sound-traversal times. The breakup into fragments (or clusters) can be roughly described by Grady's model, which balances the surface energy with the comoving (dilatational) kinetic energy of the fragments. The model predicts that the number of fragments varies as the cube root of the system population and the  $2D/3$  power of the initial pressure where  $D$  (2 or 3) is the dimensionality of the system. The molecular-dynamics results confirm these predictions within about  $\pm 0.1$  and thereby rule out three other fragmentation models. The relatively high monomer temperatures and relatively uniform fragment temperatures found here correspond to temperatures found in recent three-dimensional Lennard-Jones simulations by Vicentini, Jacucci, and Pandharipande.

## I. INTRODUCTION

The expansion of a high-pressure hot fluid into a low-pressure volume many times the original volume is a strongly nonequilibrium process. Wave propagation, fluctuations, negative pressures, surface tension, vaporization, viscosity, and heat conduction all play roles as a single-fluid mass is converted to a time-dependent collection of diverging liquid and solid fragments or clusters. A complete theoretical or computational study of such a process lies well beyond our capacity. Thus, fragmentation is primarily "understood" on the basis of experimental correlations and relatively crude "theories" (models). The expansion of an isochorically heated fluid is a challenging problem involving nonequilibrium statistical mechanics, dynamics, and fluid mechanics. Three diverse fields provide sample applications which could benefit from the ability to predict fluid fragmentation. Lithium jets in inertial confinement fusion (ICF) reactors are heated by neutrons much more rapidly than the tens of microseconds required for pressure relief.<sup>1</sup> Pressurized fluids leaving nozzles fragment.<sup>2</sup> Colliding heavy-ion beams produce compressed "nuclear matter" which exhibits fragmentation and a vapor-liquid-like phase transition.<sup>3</sup>

While fragment size is a crude description of the fragmentation process, it is useful because it is easily measured and calculated. Four hydrodynamic models have been proposed<sup>1</sup> to predict the mean fragment size. Two of these models balance fragment surface forces against pressure, either (i) the increased static pressure  $P$ , or (ii) the dynamic expansion pressure  $m\rho v^2/2$  where  $m$  is the atomic mass,  $\rho$  is the atom density, and  $v$  is the jumpoff velocity,  $P/m\rho c$ , with  $c$  indicating the sound speed. Two other models minimize the sum of the fragment surface and dilatational energies, considering (iii) the total fragment dilatational energy, or (iv) the dilatational energy near the fragment surfaces. These four models have markedly dif-

ferent dependences on the original system size and pressure.

Vaporization has also been proposed as an expansion and fragmentation mechanism. Two phase-change mechanisms are "spinodal decomposition"<sup>4</sup> and "nucleation and growth." Neither mechanism suggests any dependence of mean fragment size on original system size.

Molecular dynamics provides a test of the size-dependence predictions of the various theoretical models. Here, we apply molecular dynamics to a two-dimensional system because it can simulate relatively large radius systems, because it is easily diagnosed graphically, and because it best simulates the quasi-two-dimensional expansion of cylindrical jets in inertial fusion reactors.

## II. FRAGMENTATION MODELS

## A. Hydrodynamic models

The simplest model requires the surface tension ( $2\gamma$  or  $2\pi r\gamma$  in two or three dimensions) to balance the initial pressure,  $2rP$ , or  $\pi r^2P$ . Thus, the "fragment" or "cluster" size  $N_c$  (in atoms) is

$$N_c = \pi \left[ \frac{D+1}{D} \right]^{D-2} \rho \left[ \frac{(D-1)\gamma}{P} \right]^D, \quad (1)$$

where the dimensionality  $D$  is either 2 or 3. A more realistic model accounts for the relief of the static pressure, producing a dynamic expansion pressure and replacing  $P$  in (1) by  $m\rho v^2/2$ , where  $v$  is the jumpoff velocity,

$$N_c = \pi \left[ \frac{D+1}{D} \right]^{D-2} \rho^{D+1} [2(D-1)\gamma]^D \left[ \frac{c}{P} \right]^{2D}. \quad (2)$$

An energy-minimization model (proposed by Grady<sup>5</sup> and extended by Glenn<sup>6</sup> and Blink<sup>1</sup>) minimizes the sum of the surface-energy density plus the fragment dilatational-energy density. The surface-energy density is  $D\gamma/r$

where  $r$  is the fragment radius. For a homogeneous expansion, the dilational-energy density is  $(r\dot{\rho})^2/[2D(D+2)\rho]$  where  $-\dot{\rho}/\rho = Dv/R$ . Thus

$$N_c = \pi^{1/3} \left[ \frac{D+1}{D} \right]^{(D-2)/3} \rho^{(D+1)/3} \times [(D+2)\gamma]^{D/3} \left[ \frac{c}{P} \right]^{2D/3} N^{2/3}. \quad (3)$$

The inhomogeneity of the expansion can be partly considered by including the radial dependence of the velocity divergence. Then, the fragment radius predicted by Eq. (3) is reduced by 1 to 2 orders of magnitude for the innermost fragments,<sup>1</sup> but most of the system mass is included in fragments within a factor of 2 of the size predicted by the uncorrected Eq. (3).

If only the dilational energy in an outer shell of thickness  $\delta$  is used in the energy-minimization model,  $N_c$  is proportional to  $N$ ,

$$N_c = \left[ \frac{2\rho\gamma}{\delta} \right]^{D/2} \left[ \frac{c}{P} \right]^D N. \quad (4)$$

If Eq. (3) proves to be a more nearly correct model than Eq. (4), fragmentation must be driven by collective effects, including energy in the fragment core as well as the energy at the fragment surface.

In summary, the hydrodynamic models (1), (2), (3), and (4) predict  $N_c \sim N^0 P^{-2}$ ,  $N^0 P^{-4}$ ,  $N^{2/3} P^{-4/3}$ , and  $N P^{-2}$  respectively, in two dimensions. In three dimensions, the four models predict  $N_c \sim N^0 P^{-3}$ ,  $N^0 P^{-6}$ ,  $N^{2/3} P^{-2}$ , and  $N P^{-3}$ .

### B. Phase change as a fragmentation mechanism

It is easy to see that phase change is too slow and too weak a mechanism to drive fragmentation. For example, Fig. 1 shows the response to 800 kJ/kg of isochoric neutron heating in a 0.2-m-diam lithium jet in the HYLIFE (high-yield lithium-injection fusion-energy-converter) (Ref. 7) ICF reactor, using Young's soft-sphere equation of state.<sup>8</sup> The sudden heating causes the liquid temperature (500°C) and pressure (essentially zero) to quickly rise to 735°C and 380 MPa with no change in density (485 kg/m<sup>3</sup>). As the relief wave moves into the jet, a nearly isentropic expansion occurs. During expansion to the saturation line (and  $P_{\text{sat}} \sim 0$ ), the liquid temperature falls to 695°C, and the internal energy falls by  $\sim 16$  kJ/kg. This energy corresponds to a jumpoff velocity of about 175 m/s as internal energy is converted to kinetic energy by the tensile wave. When the expansion continues beyond zero pressure into the two-phase liquid-vapor region, phase separation or fragmentation must eventually occur, returning the fluid to the saturated liquid and vapor lines. If the isentropic expansion could continue all the way to the isentropic spinodal [where  $(\partial P/\partial V)_S$  vanishes], only 3.4 J/(kg of liquid) would be needed for equilibrium vaporization. This is about 4400 times less energy than the jumpoff kinetic energy produced by the hydrodynamic expansion. Thus, vaporization utilizes in-

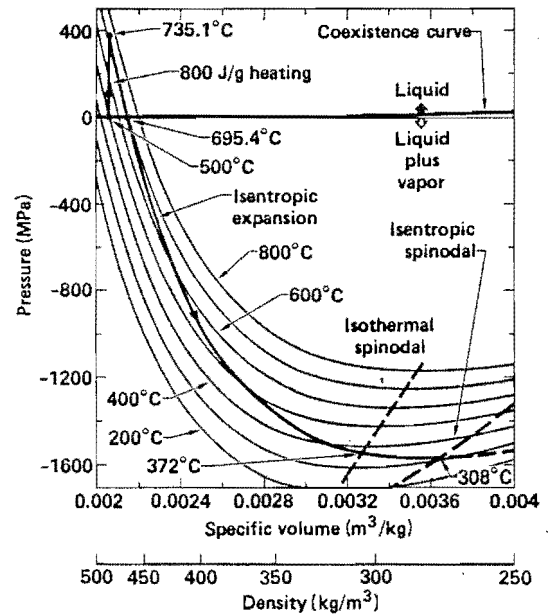


FIG. 1.  $P$ - $V$  diagram of the heating and expansion of a lithium jet. Due to the restricted specific-volume range of the diagram, the coexistence curve appears to be flat at  $\sim 0$  pressure. The critical pressure of 114 MPa is at 0.011 m<sup>3</sup>/kg (not shown). The dashed isothermal and isentropic spinodal lines cross the lower-right corner. The "two-phase" isotherms are analytic continuations of the single-phase isotherms.

sufficient energy to drive the hydrodynamic expansion and fragmentation.

It is unlikely that either spinodal line would even be approached in a real liquid-lithium ICF reactor. At the spinode, the liquid tension is  $\sim 1560$  MPa, much larger than the tensile strength of solid lithium. In an ICF reactor, the entrained gas, target debris, and corrosion products provide an abundance of potential nucleation sites. Vapor-bubble growth (by nucleation and growth) is also ineffective from a kinetic standpoint since the growth times (milliseconds) are much longer than the liquid's expansion time. Hence, it is concluded that hydrodynamic fracture is the fragmentation mechanism and that phase separation occurs later to fill the consequent voids.

### III. MOLECULAR-DYNAMICS MODEL OF FRAGMENTATION

The well-characterized Lennard-Jones 6-12 potential was used,

$$\frac{\phi(r)}{\epsilon} = 4 \left[ \left( \frac{\sigma}{r} \right)^{12} - \left( \frac{\sigma}{r} \right)^6 \right]. \quad (5)$$

The potential was truncated at  $r_t = 2.5\sigma$  to save computer time. The truncation has negligible effect on the evolution of the system, but it does allow early identification of fragment sizes. In addition, Thompson's neighbor-listing procedure<sup>9</sup> was used to reduce computer time, at some memory expense. The largest run (14 491 atoms) required a memory of 212 000 words and 6.3 sec of central processing unit time on the Cray-1 computer for each time step. In implementing Thompson's scheme a list was construct-

TABLE I. Initial conditions and results from the two-dimensional molecular-dynamics experiments. The cluster populations are indicated by  $N_c$ ,  $N_m$  is the number of monomers, and  $N$  is the original system population.

$N^a$ atoms	$kT/\epsilon$	Initial values			$c(m/\epsilon)^{1/2}$	Observed time $tc/R$	$N_c$	$N_m$	$N_c/(N-N_m)$		Translation temperature		Observed monomer temperature $kT/\epsilon$
		$\rho\sigma^2$	$P\sigma^2/\epsilon$	$c(m/\epsilon)^{1/2}$					Observed	Predicted	Observed <sup>b</sup>	Predicted	
14 491	1.01	0.61	1.02	3.7	4.4	375	1183	0.028	0.24	0.35	0.10	1.17	
2611	1.16	0.62	1.38	4.1	4.2	136	200	0.056	0.14	0.77	0.15	1.43	
2611	0.76	0.62	0.53	3.1	6.4	270	218	0.11	0.68	0.15	0.039	0.87	
2611	0.65	0.62	0.31	2.7	5.2	361	170	0.15	1.001 <sup>c</sup>	0.072	0.017	0.88	
721	1.17	0.61	1.31	4.0	6.0	44	82	0.069	0.35	0.36	0.14	1.24	
721	0.77	0.63	0.60	3.2	11.7	117	85	0.18	0.91	0.10	0.043	0.81	
721	0.65	0.65	0.40	3.2	12.0	337	66	0.515	1.5 <sup>c</sup>	0.055	0.019	0.70	
721	0.55	0.66	0.17	2.9	11.5	593	64	0.90	4.1 <sup>c</sup>	0.029	0.0037	0.59	
721	0.51	0.68	0.07	2.9	11.9	626	53	0.94	16.6 <sup>c</sup>	0.018	0.0006	0.79	
169	1.19	0.65	1.75	4.6	4.5	41	15	0.27	0.42	0.34	0.17	1.28	
169	0.77	0.68	0.86	4.0	4.5	64	7	0.43	0.82	0.067	0.051	1.15	
169	0.62	0.68	0.41	3.5	27.7	129	18	0.85	2.46 <sup>c</sup>	0.043	0.015	0.86	
169	0.50	0.73	0.11	3.6	31.2	142	15	0.92	23.8 <sup>c</sup>	0.022	0.0008	0.52	

<sup>a</sup>Including monomers.

<sup>b</sup>Ignoring monomer energy and mass.

<sup>c</sup>Adjusted to 1.0 for the graphs.

ed (for each atom) that included all atoms within some range  $r_l > 2.5\sigma$ . After the list was compiled, the cumulative scalar distances traveled by each atom were computed at each time step, and the maximum was compared to a test quantity,  $0.95[1 - 1/(n_l + 1)](r_l - 2.5\sigma)$  where  $n_l$  is the number of time steps the list has been used. The test quantity anticipated whether or not the next step would move an atom outside the list range.

The phase diagram for the two-dimensional Lennard-Jones system was established by Barker<sup>10</sup> using perturbation theory for the fluid phases and a self-consistent cell model for the solid phase. Monte Carlo calculations by Abraham<sup>11</sup> confirmed Barker's phase boundaries. Extensive equation-of-state data were compiled by Henderson<sup>12</sup> using Monte Carlo calculations. These data were used to compute the pressure and sound speed in the liquid as a function of temperature at densities near  $\rho^* = \rho\sigma^2 \sim 0.6$  (roughly midway between the critical and liquid triple-point densities). Because no data for the surface tension were available, molecular dynamics was used to calculate the size-dependent surface tension, as discussed in Sec. IV.

The initial conditions for 13 fragmentation runs are shown in Fig. 2 and tabulated in Table I. The four system sizes (169, 721, 2611, and 14491 atoms) correspond to crystals in the shape of regular hexagonal crystals with 8, 16, 30, and 70 rows of particles on a side. These configurations were used to initiate the runs. (Each crystal was melted and equilibrated to approximately the desired temperature and density within a confining wall; the fragmentation runs began when the wall was removed.)

Verlet's algorithm, with a time step  $\Delta t$  of  $\sim 0.02$ , in units of  $(m\sigma^2/\epsilon)^{1/2}$ , was used,

$$\mathbf{r}_+ = 2\mathbf{r}_0 - \mathbf{r}_- + \mathbf{F}_0(\Delta t)^2/m \quad (6)$$

where  $\mathbf{r}_-$ ,  $\mathbf{r}_0$ , and  $\mathbf{r}_+$  are the atom locations at three successive times, and  $\mathbf{F}_0$  is the total force from all atoms within  $2.5\sigma$ . Velocities were obtained from the coordinates,

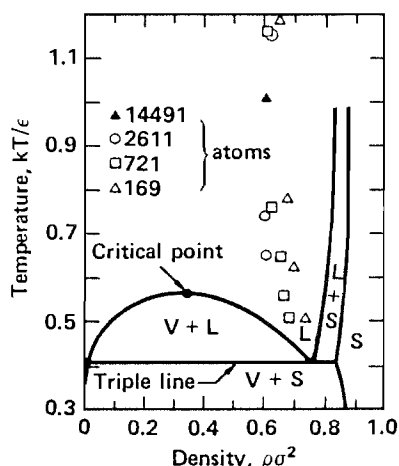


FIG. 2. Initial conditions for the 13 molecular-dynamics fragmentation simulations.

$$v_0 = (\mathbf{r}_+ - \mathbf{r}_-)/2\Delta t \quad (7)$$

The potential, translational, rotational, and thermal energies and the fragment sizes were tabulated. Fragment translational temperatures were defined as the fragment's center-of-mass kinetic energy in the fixed frame of reference divided by the product of Boltzmann's constant  $k$  and the corresponding fragment's size (in atoms). Fragment rotational temperatures were defined as  $L^2/kN_c I$  where  $L$  is the angular momentum around the fragment center and  $I$  is the moment of inertia. Fragment thermal temperatures were given by the remaining kinetic energy divided by the product of  $k$  and the corresponding fragment's size.

## IV. RESULTS

### A. Two-dimensional surface tension

Recently, Thompson, Gubbins, Walton, Chantry, and Rowlinson<sup>13</sup> published an extensive molecular-dynamics study of three-dimensional surface tension that used time averages of up to  $t^* = t(m\sigma^2/\epsilon)^{1/2} = 1400$ . To extend Thompson's study to two dimensions, a series of molecular-dynamics calculations was performed on systems ranging from 70 to 700 atoms at reduced temperatures ( $T^* = kT/\epsilon$ ) below, near, and above the triple point. Density and (Irving-Kirkwood) pressure-tensor time averages were taken for up to  $t^* = 1450$  in a few cases, with typical averaging periods being for  $t^* = 400-700$ . Analysis of the results indicates that the runs below the triple point did not reach equilibrium. (Low densities and negative pressures typical of the two-phase solid-vapor region were measured.) For the higher-temperature runs ( $T^* = kT/\epsilon \sim 0.45$ ), fluctuations and occasional drop fragmentation obscured the results. Only near the triple point were reasonable time-averaged pressure-tensor profiles obtained.

The surface tension measured at the proper radius  $R_s$  (which is significantly different from the equimolar radius for small drops), is<sup>1</sup>

$$\gamma = \int_0^\infty (P_N - P_T) \left[ \frac{r}{R_s} \right]^{D-1} dr, \quad (8)$$

where  $D$  is, again, the dimensionality (2 or 3),  $P_N$  and  $P_T$  are the normal and tangential components of the pressure tensor, and the zero of  $r$  is within the bulk of the fluid (where  $P_N = P_T$ ). The integrand is nonzero only near the interface. The normal and tangential components are related by a force balance, leading to

$$P_N - P_T = - \left[ \frac{r}{D-1} \right] \left[ \frac{\partial P_N}{\partial r} \right], \quad (9)$$

in two or three dimensions. Finally, the Laplace equation is used to eliminate  $R_s$ ,

$$\Delta P = P_N(\text{liquid}) - P_N(\text{vapor}) = \frac{(D-1)\gamma}{R_s}. \quad (10)$$

The result is

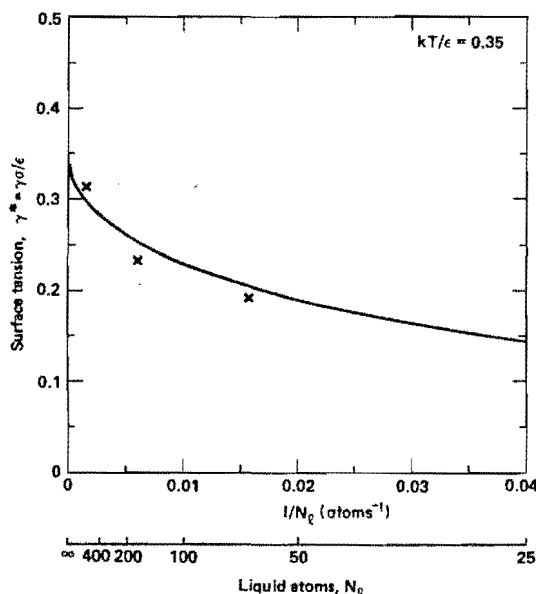


FIG. 3. Two-dimensional surface tension at  $kT/\epsilon=0.35$  from molecular-dynamics calculations.

$$\gamma = - \left[ \frac{\Delta P^{D-1}}{(D-1)^D} \right] \int_0^\infty \frac{\partial P_N}{\partial r} r dr, \quad (11)$$

in two or three dimensions. The resulting surface tension at  $T^*=0.35$  is plotted in Fig. 3 as a function of  $1/N_l$ , where  $N_l$  is the number of liquid atoms in the drop. For interpolation, we assume that the surface tension decreases linearly with temperature to zero at the critical point, and that it also falls to zero for a single-atom system,

$$\gamma = 0.35(1 - N_l^{-1/2})^4 \left[ 1 - \left[ \frac{T^* - 0.35}{0.21} \right] \right] (\epsilon/\sigma). \quad (12)$$

A simple scaling model based on excess energy due to missing bonds for surface atoms produced<sup>1</sup> reasonable agreement between the two-dimensional data and Thompson's three-dimensional results.

#### B. Fragment size as a function of system size and pressure

Fragment sizes were usually tabulated after only a few sound-traversal times in order to minimize the influence of vapor-pressure formation (Table I). In cases where fragmentation was marginal, much more time elapsed before fragmentation. Examination of the atomic-position plots for such cases indicates that some regions oscillated (changed overall shape) several times before fragmenting.

The fragment sizes (in atoms) from two 2611-atom runs are shown in Fig. 4. The largest fragment, the average of the ten largest fragments, and the average of the largest fragments comprising 30% of the nonmonomer population are shown. In each case, the raw data have been slightly adjusted (using the energy-minimization model, model 3) to uniform initial conditions [2611 nonmonomer atoms,  $\rho^*=0.6$ ,  $c^*=c(m/\epsilon)^{1/2}=4.0$ , and  $\gamma^*=0.32$ ]. The only remaining variable in model 3 is the initial pressure.

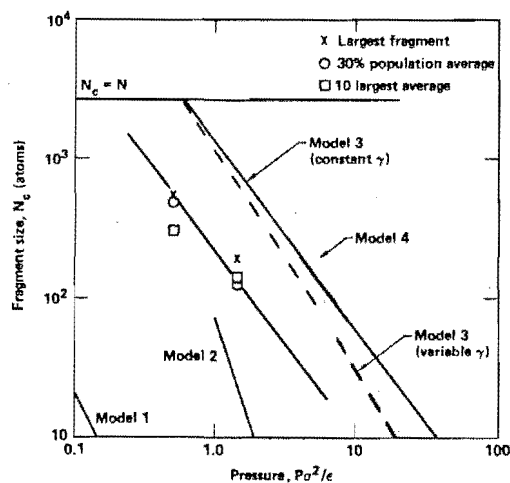


FIG. 4. Observed and predicted fragment sizes (atoms) as a function of initial pressure, for two 2611-atom simulations. The data and model predictions have been slightly adjusted to constant initial conditions. The model numbers refer to Eqs. (1)–(4). The three observed values for each simulation are for the largest fragment, the average of the ten largest fragments, and the average of the largest fragments comprising 30% of the system population (less monomers).

The slopes of the three fragment-size curves are  $-1.03$ ,  $-0.86$ , and  $-1.42$ , respectively; these values bracket the predicted slope of  $-\frac{4}{3}$  from model 3 reasonably well. To illustrate the sensitivity of the fragmentation to fragment-size-dependent surface tension, the prediction curve is also shown using the lower surface tensions at the actual fragment sizes; the “observed” curves would be similarly steeper when the surface-tension correction (to  $\gamma^*=0.32$ ) is eliminated. Finally, the other model predictions are shown. The slopes of models 1, 2, and 4 ( $-2$ ,  $-4$ , and  $-2$ , respectively) are much steeper than the molecular-dynamics results.

The fragment sizes from the highest-pressure run for each system size (14 491, 2611, 721, and 169 atoms) are shown in Fig. 5. The nomenclature is identical to that of the previous figure. As in Fig. 4, the data were slightly adjusted to uniform initial conditions ( $P^*=P\sigma^2/\epsilon=1.4$ ,  $\rho^*=0.6$ ,  $c^*=4.0$ , and  $\gamma^*=0.32$ ). The only remaining variable in the models is the system size  $N$  (total number of particles). The slopes of the middle section of the three fragment-size curves are 0.75, 0.69, and 0.64, respectively. These observed values bracket the predicted slope of  $\frac{2}{3}$  from model 3. The 169-atom data were not used to compute the slope because of minimal fragmentation. The 14 491-atom fragment sizes are probably a bit low. Position snapshots and density profiles indicate that a sloshing motion was present in the system at the time the confining boundary was removed. However, if the slopes are computed using line segments between the 721- and 14 491-atom data, the results are 0.54, 0.50, and 0.41, respectively. Thus, the molecular-dynamics results indicate a possible system-size dependence of the  $\frac{2}{3}$  power (the illustrated line), but support that slope with an uncertainty of  $\pm 0.15$ . This result again is consistent with the

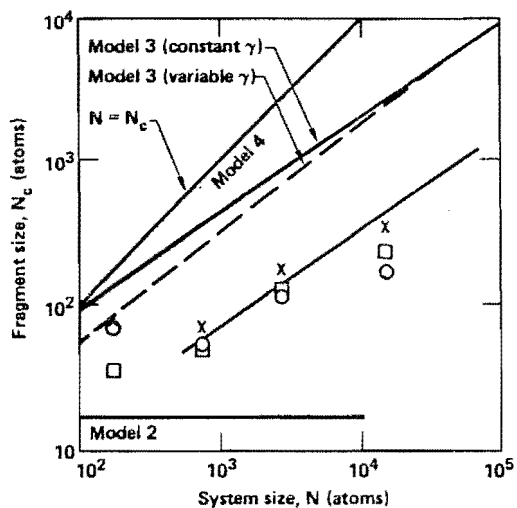


FIG. 5. Observed and predicted fragment sizes (atoms) as a function of system size, for similar heating levels. The nomenclature is identical to Fig. 4.

energy-minimization model (model 3). Models 1 and 2 include no system-size dependence and accordingly predict very low fragment sizes for this initial condition (0.1 and 18 atoms, respectively). Model 4 predicts a much steeper slope (1.0) than found in the molecular-dynamics runs.

Although the data in Figs. 4 and 5 support the energy-minimization model's power-law dependence of fragment size on system size and isochoric heating level (initial pressure), the magnitudes of the observed sizes (in atoms) are about ten times lower than the model-3 prediction.

### C. Time evolution of the system

As time evolved in the thirteen numerical experiments, snapshots of the atomic positions were used to visualize the fragmentation; a sample sequence is shown in Fig. 6.

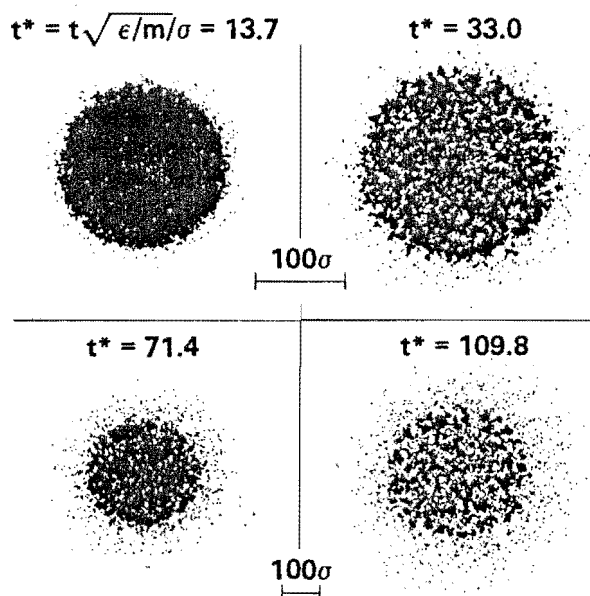


FIG. 6. Snapshots of the atomic configurations at four times during the fragmentation process of a 14491-atom system ( $kT/\epsilon \sim 1.0$ ).

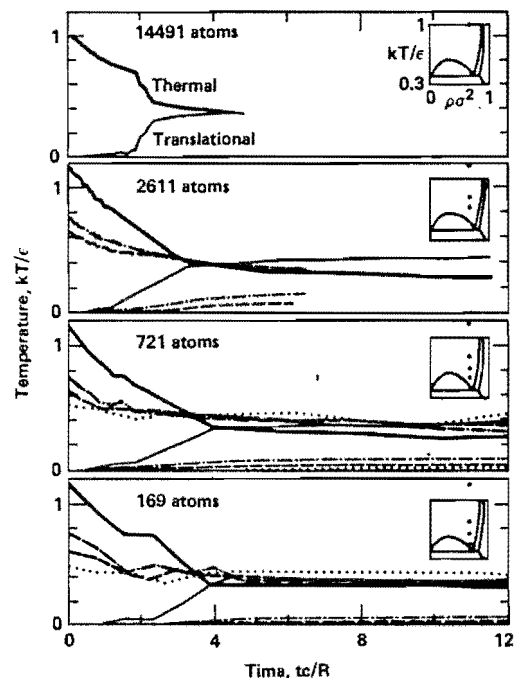


FIG. 7. Thermal- and translational-temperature evolution in the fragmentation simulations.

Inspection of this figure indicates that the average fragment size is smallest near the system center, in agreement with model 3 when the variation of velocity divergence with radius is considered.

A more quantitative description of the fragmentation process is contained in Table I and in Figs. 7 and 8 which show the translational and thermal temperatures and the largest cluster size as functions of time, system population, and initial temperature. The abscissa of each plot,  $tc/R$ , is the time divided by the sound-traversal time. The initial temperature corresponds to the y intercepts in Fig. 7. To decrease the influence of vapor-pressure formation on the results, both thermal and translational tem-

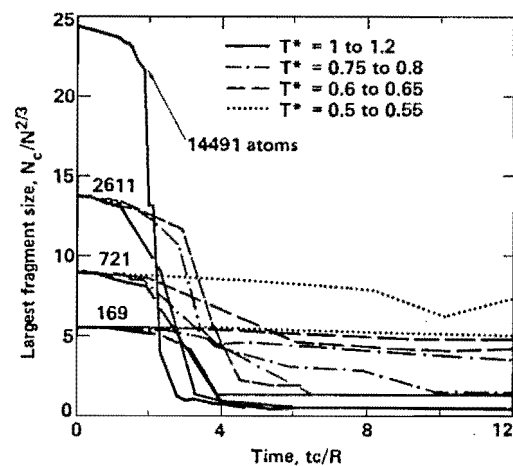


FIG. 8. Size of the largest cluster as a function of time in the two-dimensional fragmentation simulations. The ordinate is scaled according to model 3 to eliminate the system-size dependence.

peratures are based on the total number of nonmonomer atoms in the system. The rotational temperature was not plotted because it was always negligibly small.

The thermal temperature typically relaxes to a "post-fragmentation" level of about 0.35–0.4 (near the triple point) after two or three pressure-relief times ( $R/c$ ) (Fig. 7). The translational temperature reaches its "postfragmentation" value at about the same time, but this value depends on the initial temperature. For the highest initial-temperature level ( $T^* \sim 1.15$ ), the final translational temperature was  $\sim 0.4$ , somewhat higher than the final thermal temperature. For the lower initial temperatures, the final translational temperature was 0.1 or lower. As predicted by model 3, there was an observable system-size dependence for the translational temperature, with the larger systems attaining higher values. The total of the final translational and thermal temperatures was always less than the initial thermal temperature; the remaining energy was either carried as kinetic energy by monomer atoms in the vapor, or stored as potential energy in the fragments. The system potential energy increases due to bond breaking during vaporization and surface-area growth (fragmentation), and decreases slightly due to the increase in bulk density caused by the lower liquid temperature.

The evolution of the largest cluster size is shown in Fig. 8. The ordinate is scaled by  $1/N^{2/3}$  to remove the system-size dependence predicted by model 3. When it was widespread, fragmentation typically occurred at about two to four sound-traversal times. The  $T^* \sim 0.75$  experiments appear to be borderline for the three smallest system sizes, with fragmentation occurring in steps over an

extended period of time much longer than a few sound-traversal times.

The paths followed on a  $T$ - $\rho$  diagram are shown in Fig. 9 for two 2611-atom runs. The paths shown use spatially averaged densities up to the fragmentation point, but inspection of the position plots shows marked heterogeneity much earlier. (The definition of fragmentation used here requires a minimum fragment separation of  $2.5\sigma$ ). Internal voids which eventually become fragment surfaces appear much earlier. The internal voids decrease the "prefragment" average density; hence, density appears to increase upon fragmentation. Temperature also decreases; as a new daughter fragment is born, its center-of-mass translational energy is instantaneously subtracted from the "internal" energy of its parent cluster. Most of the fragment temperatures lie along the saturated-liquid-phase line. Finally, although the low-temperature run appeared to penetrate the unstable region under the isothermal spinodal (and may have reached the isentropic spinodal which lies below the isothermal spinodal), the regular density patterns<sup>14</sup> characteristic of spinodal decomposition were not observed. This is because the fragmentation expansion is inhomogeneous. If the internal voids that precede fragmentation were not included in the density calculation, then the spinodal lines would not be reached.

#### D. Fragment-size distribution

The integrated (cumulative) population distributions for three experiments with similar heating levels and varying system sizes are shown in Fig. 10. The smallest (721-atom) system has a significant portion of the population concentrated in an intermediate fragment-size range (indi-

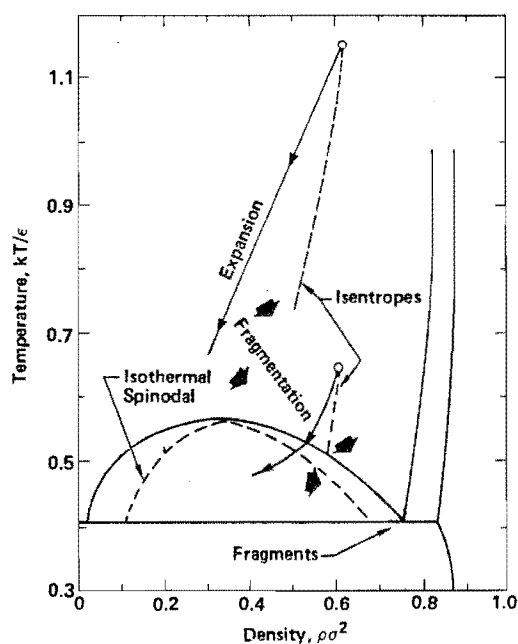


FIG. 9. Pressure-density paths followed by two fragmentation simulations. The densities were calculated in an average sense; actual local density in the fluid did not reach such low values. Most of the fragments had densities and temperatures characteristic of saturated liquid cooler than the saturation temperature associated with the initial density. This cooling was probably due to the formation of vapor pressure.

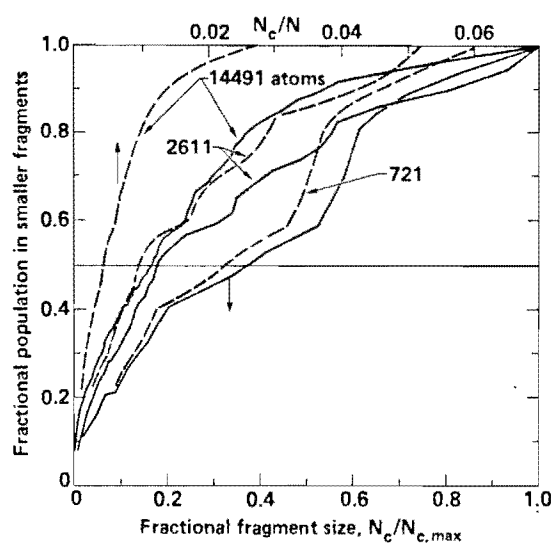


FIG. 10. Integrated population distributions as a function of fragment size for three fragmentation runs with similar heating levels but different system sizes. The dashed lines give integrals as functions of the fractional fragment size  $N_c/N$  and the solid lines are normalized to the largest fragment size, i.e., the abscissa is  $N_c/N_{c,max}$ . The fragment data were taken just as fragment sizes became well defined.

cated by the steep portion of the curve). The larger systems' populations were peaked at relatively lower fragment sizes and exhibited decreasing population density with increasing fragment size. The overall effect of increasing system size was to concentrate population in smaller fractional fragment sizes; 50% of the population was in fragments smaller than 36%, 18%, and 17% of the largest fragment size for the 721-, 2611-, and 14491-atom systems, respectively.

### E. Translational energy of the fragments and monomers

The translational temperatures (ignoring monomer energy and mass) are shown in Fig. 11 as a function of system size and initial pressure. The inset shows the observed translational temperatures which properly increase with heating level (initial pressure). All the values exceed  $mv^2/2k$ , where  $v$  is the jumpoff velocity (dashed line). In two dimensions, model 3 predicts<sup>1</sup>

$$T_{tr} = \left[ \frac{mv^2}{2k} \right] \left[ 1 - \frac{1}{2} \frac{N_c}{N} \right]. \quad (13)$$

For extreme fragmentation ( $N_c \rightarrow 0$ ), Eq. (13) produces the correct upper bound, but for no fragmentation Eq. (13) predicts  $\frac{1}{2}$  the upper bound, rather than zero. The failure at no fragmentation is a consequence of the assumption of a homogeneous expansion in model 3.

The main portion of the figure shows the ratio of the observed to the predicted [Eq. (13)] translational temperatures. The additional kinetic energy is from two sources: vapor-pressure formation (which is limited in Fig. 11 by the elimination of monomers from the calculation), and fragmentation due to fluctuations (a phenomenon observed for small systems on the saturation line with no isochoric heating).

For macroscopic systems, model 3 suggests that both vapor-pressure formation and fracture due to "equilibrium" fluctuations are negligible. Glenn's three-dimensional (macroscopic) hydrodynamic code calculations<sup>6</sup> confirmed the upper bound of  $mv^2/2k$  when no tension is allowed in the material. Our molecular-dynamics calculations (Fig. 11) show that the translational temperature tends to increase with system size, at least for systems of a few thousand atoms or less. However, the 14491-atom result shows a decreased translational tem-

perature with increasing system size (even though its initial sloshing motion would be expected to produce more translational energy than an initially quiescent system). Thus, these limited molecular-dynamics results are not inconsistent with model 3. Finally, we note that the peak in the excess translational temperature is in the region of the critical nucleus size. Systems smaller than the critical size are naturally unstable, leading to fragmentation even in saturated systems.

The monomer temperatures at the time of fragmentation for each run are listed in the last column of Table I. The average liquid temperature during the monomer formation period lies somewhere between the peak listed in the second column of the table and the saturation temperature ( $\sim 0.5$ ). The monomer temperature exceeds both the average and the peak liquid temperatures in every case. Similar results have been found by Vicentini, Jacucci, and Pandharipande<sup>15</sup> using three-dimensional molecular dynamics for systems of 250 atoms. Vicentini, Jacucci, and Pandharipande also observed that the thermal temperatures of most of the fragments are similar and essentially independent of the initial heating level, in agreement with our results.

## V. CONCLUSIONS

Two-dimensional molecular-dynamics fragmentation simulations were performed for five levels of heating and four system sizes. The numerical experiments produced agreement with only one of four proposed models (the energy-minimization model, model 3). The model's power-law dependence of fragment size (atoms) on system size ( $\frac{2}{3}$ ) and initial pressure ( $-\frac{4}{3}$ ) were both supported by the data. The larger fragment sizes were about an order of magnitude smaller than the model-3 predictions. There was an unexpectedly large level of translational energy generated in these molecular-dynamics runs, probably due to the combination of small system size (fluctuations) and near-critical saturation temperature (vaporization). In macroscopic systems, model 3 (with the 0.1 correction factor) predicts

$$r = \left[ \frac{D+2}{\rho} \gamma \left[ \frac{c}{\Gamma e} \right]^2 \right]^{1/3} 10^{-1/D} R^\alpha \quad (14)$$

where  $r$  is the fragment radius,  $R$  is the system radius,  $D$  is the number of dimensions (2 or 3),  $\Gamma$  is the Grüneisen parameter,  $e$  is the added heat per unit mass,  $\rho_m$  is the mass density, and  $\alpha = 0.583 \pm 0.083$  ( $\frac{1}{2}$  to  $\frac{2}{3}$ ). When Eq. (14) is applied to the HYLIFE (ICF) reactor initial conditions (two dimensions, 0.1-m-radius lithium jets, 800 kJ/kg added energy, 485 kg/m<sup>3</sup> density, 1.0 Grüneisen parameter, 0.35 J/m<sup>2</sup> surface tension, and 4500 m/s sound speed), the predicted fragment-radius range is 0.3–0.45 mm. Thus, fragmentation will produce more than a 2 orders-of-magnitude increase in the surface area, making it plausible that the required pulse rate of 1.5 Hz can be achieved.

Grady<sup>5</sup> obtained excellent agreement between the *uncorrected* version of Eq. (14) and fragmentation experiments with oil shale and steel. He used fracture data to estimate surface energy, thereby predicting much larger

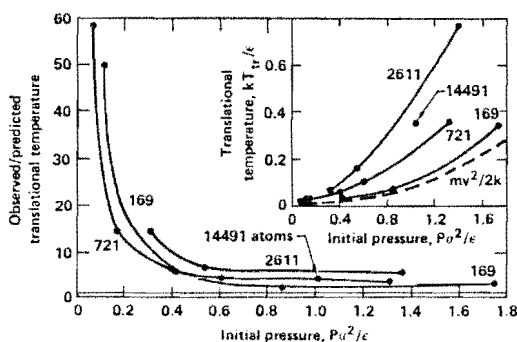


FIG. 11. Translational temperatures (scaled to the prediction of model 3) for the 13 molecular-dynamics simulations.

fragments than would be obtained using the surface energies for clean cleavage cracks. If we were to use fracture data to estimate the surface tension, the discrepancy with the molecular-dynamics results would become even worse. We have no quantitative argument to account for our tenfold-smaller fragment sizes. Evidently a part of the initial heat energy (which greatly exceeds the kinetic energy of dilation) contributes to fragmentation in hot fluids. An analysis of the catastrophic fragmentation of compressed cold crystals would be a useful complement to the fluid simulations.

#### ACKNOWLEDGMENTS

This work was performed under the auspices of the U.S. Department of Energy by the Lawrence Livermore

National Laboratory (LNLL) under Contract No. W-7405-Eng-48. One of us (J.A.B.) appreciates the support of the Lawrence Livermore National Laboratory Laser Program and the Veterans Administration. Discussions with Jack Hovingh of LLNL and both Farid Abraham and John Barker of IBM were particularly helpful. W.G.H. thanks the Air Force Office of Scientific Research and the Academy of Applied Science for the partial support of visits to the Università di Trento, Italy, and the Materials Research Laboratory of the University of Illinois (Urbana-Champaign). Discussions with Professor Gianni Jacucci were particularly helpful. His hospitality (at Trento) and Professor Peter Flynn's and Dr. Giulia DeLorenzi's (at Urbana-Champaign) were especially appreciated.

- 
- <sup>1</sup>J. A. Blink, Ph.D. thesis, University of California at Davis/Livermore, 1984.
- <sup>2</sup>R. D. Reitz and F. V. Bracco, *Phys. Fluids* **25**, 1730 (1982).
- <sup>3</sup>H. Schulz, B. Kämpfer, H. W. Barz, G. Röpke, and J. Bondorf, *Phys. Lett.* **147B**, 17 (1984).
- <sup>4</sup>J. H. Cahn, *Trans. Metall. Soc. AIME* **242**, 166 (1968).
- <sup>5</sup>D. E. Grady, *J. Appl. Phys.* **53**, 322 (1982).
- <sup>6</sup>L. A. Glenn, Lawrence Livermore National Laboratory Report No. UCID-19737, 1983 (unpublished).
- <sup>7</sup>M. J. Monsler, J. Hovingh, D. L. Cook, T. G. Frank, and G. A. Moses, *Nucl. Technol.* **1**, 302 (1982), Sec. IX. See also Lawrence Livermore National Laboratory Laser Program Annual Reports for 1978, 1979, 1980, and 1981 (unpublished, No. UCRL-50021-year, where year is '78, '79, '80, or '81).
- <sup>8</sup>D. A. Young, Lawrence Livermore National Laboratory Report No. UCRL-52352, 1977 (unpublished).
- <sup>9</sup>S. M. Thompson, *Information Quarterly for MD&MC Simulations* (Daresbury Laboratory, Daresbury, England, 1983), Vol. 8, p. 20.
- <sup>10</sup>J. A. Barker, D. Henderson, and F. F. Abraham, *Physica (Utrecht)* **106A**, 226 (1981).
- <sup>11</sup>F. F. Abraham, *Phys. Rep.* **80**, 339 (1981). This reference also contains a large bibliography of two-dimensional simulation studies.
- <sup>12</sup>D. Henderson, I. Snook, and R. O'Wallaby Watts, *Mol. Phys.* **34**, 301 (1977).
- <sup>13</sup>S. M. Thompson, K. E. Gubbins, J.P.R.B. Walton, R.A.R. Chantry, and J. S. Rowlinson, *J. Chem. Phys.* **81**, 530 (1984).
- <sup>14</sup>F. F. Abraham, *Phys. Rep.* **53**, 93 (1979).
- <sup>15</sup>A. Vicentini, G. Jacucci, and V. R. Pandharipande, *Phys. Rev. C* **31**, 1783 (1985).